

Manuscript version: Author's Accepted Manuscript

The version presented in WRAP is the author's accepted manuscript and may differ from the published version or Version of Record.

Persistent WRAP URL:

<http://wrap.warwick.ac.uk/160266>

How to cite:

Please refer to published version for the most recent bibliographic citation information. If a published version is known of, the repository item page linked to above, will contain details on accessing it.

Copyright and reuse:

The Warwick Research Archive Portal (WRAP) makes this work by researchers of the University of Warwick available open access under the following conditions.

Copyright © and all moral rights to the version of the paper presented here belong to the individual author(s) and/or other copyright owners. To the extent reasonable and practicable the material made available in WRAP has been checked for eligibility before being made available.

Copies of full items can be used for personal research or study, educational, or not-for-profit purposes without prior permission or charge. Provided that the authors, title and full bibliographic details are credited, a hyperlink and/or URL is given for the original metadata page and the content is not changed in any way.

Publisher's statement:

Please refer to the repository item page, publisher's statement section, for further information.

For more information, please contact the WRAP Team at: wrap@warwick.ac.uk.

High-Dimensional Feature based Non-Coherent Detection for Multi-Intensity Modulated Ultraviolet Communications

Wenxiu Hu, Min Zhang, Zhe Li *Member, IEEE*, Sergei Popov, *Member, IEEE, Fellow, OSA*,
Mark Leeson, *Senior Member, IEEE*, Tianhua Xu *Member, IEEE*

Abstract—Ultraviolet communication (UVC) has been regarded as a promising supplement for overloaded conventional wireless communications. One challenge lies in the communication deterioration caused by the UV-photon scattering induced inter-symbol-interference (ISI), which will be even worse when encountering multilevel pulse amplitude modulation (multi-PAM) symbols. To address this ISI, traditional coherent detection methods (e.g., maximum-likelihood sequence detection, MLSD) require high computational complexities for UV channel estimation and sequential detection space formation, thereby making them less attractive. Current non-coherent detection, which simply combines the ISI-insensitive UV signal features (e.g., the rising edge) into a one-dimensional (1D) metric, cannot guarantee reliable communication accuracy. In this work, a novel high-dimensional (HD) non-coherent detection scheme is proposed, leveraging a HD construction of the ISI-insensitive UV signal features. By doing so, we transform the ISI caused sequential detection into an ISI-released HD detection framework, which avoids complex channel estimation and sequential detection space computation. Then, to compute the detection surface, a UV feature based unsupervised learning approach is designed. We deduce the theoretical bit error rate (BER), and prove that the proposed HD non-coherent detection method has a lower BER than that of the current 1D non-coherent scheme. Simulation results validate our results, and more importantly, demonstrate a BER that approaches that of the state-of-the-art coherent MLSD ($< 1\text{dB}$ in SNR at $\text{BER} = 4.5 \times 10^{-3}$, the 7% overhead forward-error-correction limit), and also a reduction of computational complexity by at least two orders of magnitude.

Index Terms—Ultraviolet communications, inter-symbol interference, unsupervised learning, non-coherent detection.

I. INTRODUCTION

Attributed to its solar-blind and non-line-of-sight (NLoS) properties, ultraviolet communication (UVC) has been regarded as a promising candidate for sharing the steeply rising demands of conventional wireless communication systems

[1]–[5]. Key research areas include, *inter alia*, UVC device designs [6]–[9], channel modelling [4], [10]–[14], coding/modulation [15]–[17], and signal detection designs [18]–[23].

From a fundamental perspective, one challenge that causes the deterioration of the communication performance is inter-symbol-interference (ISI), which is induced by the strong UV photon scattering phenomenon, and will cause delaying and multi-path effects that contaminate the received signals [19], [21], [23]. This will be even worse when multi-amplitude/intensity modulation schemes are employed, for example, the M th symbol in $M > 2$ -level pulse amplitude modulation (M -PAM) will amplify the long-tail channel impulse response (CIR) which strengthens the ISI contamination [15].

To address this, coherent signal detection schemes have been widely studied and designed, leveraging an exact estimation of CIR to compute the channel state information (CSI) for ISI compensation and signal detection [19]–[22], [24]. The state-of-the-art maximum likelihood sequence detection (MLSD), i.e., maximizing the sequentially conditioned likelihoods for signal detection, has been proved to obtain the optimal bit error rate (BER) with accurate CIR acquisition [19]. However, the scheme is less attractive when addressing long-tail intensive ISI (say with ISI length L and M -PAM modulation), due to the high computational complexity caused by (i) the computations of M^L likelihood functions for each symbol, and (ii) the complex Viterbi-like implementation. Other less computational particle-filtering approximations of MLSD [21], [24] require either a heavy likelihood computation burden given the large number of particles for approximation, or deliver poor detection accuracy for insufficient particle numbers.

Alternatively, non-coherent detection schemes have been proposed and researched in [18], [25]–[27], whose ideas are to transform the ISI induced sequential detection space into an ISI-released binary detection framework, thereby avoiding the aforementioned high computational CSI estimation and sequential signal detection. Whilst these approaches offer low computational demands, their accuracy is severely compromised. For example, the work in [18], [25] illustrates BER saturation when facing intensive ISI. In our previous work [23], four ISI insensitive features of the UV signals’ geometric shapes (such as rising edge and inflexion) were extracted and exploited, showing reliable performance in counteracting intensive ISI. However, the linear combination of the features

This work is supported by EU Horizon 2020 Grant (No. 101008280), Swedish Research Council (Vetenskapsrådet 2019-05197) and RISE SK. M. Zhang is supported by China NSFC Grant 61975020. (*Corresponding author* : Tianhua Xu) W. Hu and M. Leeson are with School of Engineering, University of Warwick, Coventry CV4 7AL, United Kingdom. T. Xu is with School of Engineering, University of Warwick, Coventry CV4 7AL, United Kingdom, with Tianjin University, Tianjin 300072, China and also with University College London (UCL), London WC1E 6BT, United Kingdom. (tianhua.xu@ieee.org) M. Zhang is with Institute of Information Photonics and Optical Communications, Beijing University of Posts and Telecommunication, Beijing 100876, China (mzhang@bupt.edu.cn). Z. Li is with II-VI Incorporated, Horsham, PA 19044, United States (zhe.li@ieee.org). S. Popov is with KTH Royal Institute of Technology, Stockholm 16440, Sweden (sergeip@kth.se).

does not fully employ the signal's properties and results in a high BER, e.g., a $> 5\text{dB}$ loss in SNR when compared with the coherent MLSD method (see Fig. 4).

In this work, we propose a high-accuracy non-coherent detection scheme with a low-computational burden, leveraging a high-dimensional (HD) construction of the UV signals' geometric features that are insensitive to the ISI contamination. Compared with the coherent sequential detection schemes [19]–[21], the proposed scheme does not require heavy computational operations for exact CIR estimation and sequential likelihood computation. Compared to the current non-coherent schemes [18], [23], [25]–[27], the constructed HD feature is ISI-insensitive and can provide lower BER for signal detection (see theoretical proof in Section III. C), which thereby guarantees better accuracy performance.

The rest of the paper is structured as follows. In Section II, we describe the UVC model, along with the problem formulation. In Section III, we elaborate our proposed HD non-coherent detection scheme, and compute its theoretical BER. The simulation results are provided in Section IV. We finally conclude the work in Section V.

II. SYSTEM MODELS AND PROBLEM FORMULATION

A generic UVC system is composed of a UV transmitter (Tx), the wireless UV channels, and a UV receiver (Rx), which is shown in Fig. 1(a). In the Tx, the binary input is modulated by the $M \in \mathbb{N}^+$ pulse amplitude modulation (M-PAM), which then will be converted to different intensities of UV photons for transmission. By denoting the k th M-PAM modulated symbol as $s_k = m \in \{0, 1, \dots, M-1\}$, the transmitted signal $s(t)$ over time t in terms of the number of UV photons is expressed as:

$$s(t) = \sum_{k=1}^{\infty} s_k \cdot \delta(t - kT_b) \otimes c(t). \quad (1)$$

In Eq. (1), T_b is the symbol interval, $\delta(t - kT_b)$ accounts for the Dirac delta function at $t = kT_b$, \otimes denotes the convolution operator, and $c(t) = N_T/T_p \cdot \text{rect}((t - T_p/2)/T_p)$ is the rectangular pulse shape of the UV-LED, with T_p the pulse width, and N_T the transmitted number of UV photons for a single-level symbol (i.e., $s_k = 1$).

Then, the UV signal $s(t)$ will be transmitted through the wireless UV channel. As seen in Fig. 1(a), the UV CIR, denoted as $h(t)$, shows a long tail nature given the NLoS UV photon scattering. $h(t)$ is governed by the Tx-Rx distance r , the Tx's beam divergence θ_T and apex angle β_T , the Rx's half-field of view θ_R and apex angle β_R , and the atmospheric parameters [11], [12]. In this work, $h(t)$ is simulated via the Monte-Carlo process as discussed in [10], [11]. The exact form of $h(t)$ is unnecessary to non-coherent detection schemes, while it has to be accurately estimated in coherent detection approaches.

At the Rx, the photon detector (e.g., photomultiplier tube, PMT [1]) firstly converts the received photons into electrical voltages, which then pass through the sampling oscilloscope to derive discrete signals. As we assign the sampling interval as $T_s = T_b/J$ (i.e., J samples are collected for k th symbol),

the discrete received signal can be expressed via the linear time-invariant (LTI) model [19], [23]:

$$y_i = \underbrace{h_{i-(k-1)J} \cdot s_k}_{\text{current signal}} + \underbrace{\sum_{l=k-L+1}^{k-1} h_{i-(l-1)J} \cdot s_l}_{\text{ISI}} + \underbrace{\epsilon_i}_{\text{noise}}. \quad (2)$$

In Eq. (2), y_i is the received signal at time $t = iT_s$, $i \in \{(k-1)J+1, \dots, kJ\}$, so we have the $[i - (k-1)J]$ th discrete signal sample for k th symbol. $h_{i-(l-1)J}$ is the discrete UV CIR coefficient, accounting for the electrical voltage corresponding to the mean number of the received UV photons emitted at the l th symbol interval [23], i.e., $h_{i-(l-1)J} = \int_{(i-(l-1)J-1)T_s}^{(i-(l-1)J)T_s} h(t) \otimes c(t) dt$. $\epsilon_i \sim \mathcal{N}(\mu, \sigma^2)$ represents Gaussian noise, which is comprises the sum of dominant device induced Gaussian noise and subordinate Poisson distributed photon counting noise [23].

Given the expressions of the received signals in Eq. (2), the aim of this work is to detect the current M-PAM s_k from the received signals y_1, \dots, y_{kJ} . The main challenge lies in how to combat the ISI with the unknown CIR coefficients $h_{i-(l-1)J}$, which, if multiplied by the multi-PAM symbols, i.e., $h_{i-(l-1)J} \cdot s_l$, makes the ISI more severe. To cope with this, coherent detection schemes (e.g., MLSD [19], [20] and particle-filter methods [21]) demand heavy pilot overheads for CIR estimation, and high computational complexity to search the M^L symbol space for *a posteriori* computation and symbol detection (given M-PAM with L length ISI). Non-coherent schemes are all designed for binary inputs [23], [28], and offer poor detection accuracy when dealing with multi-symbol detection (we show this in Fig. 5). This thereby motivates us to design a pilot-less, computationally efficient and more reliable non-coherent detection scheme for M-PAM UVC systems.

III. HIGH-DIMENSIONAL NON-COHERENT DETECTION

In this section, we elaborate our proposed HD feature based non-coherent detection. This contains (i) the construction of HD UV features, and (ii) the unsupervised learning (clustering) and signal detection under UV feature based constraints. Then, we will compute and compare the theoretical symbol error rate (SER) from this proposed HD non-coherent scheme with the current 1D method in [23].

A. High-dimensional Feature Construction

We construct a D -dimensional feature space \mathbb{R}^D via our previously designed UV sub-features, i.e.,

$$\mathbf{z}_k = [z_{1,k}, z_{2,k} \dots, z_{D,k}]^T \in \mathbb{R}^D. \quad (3)$$

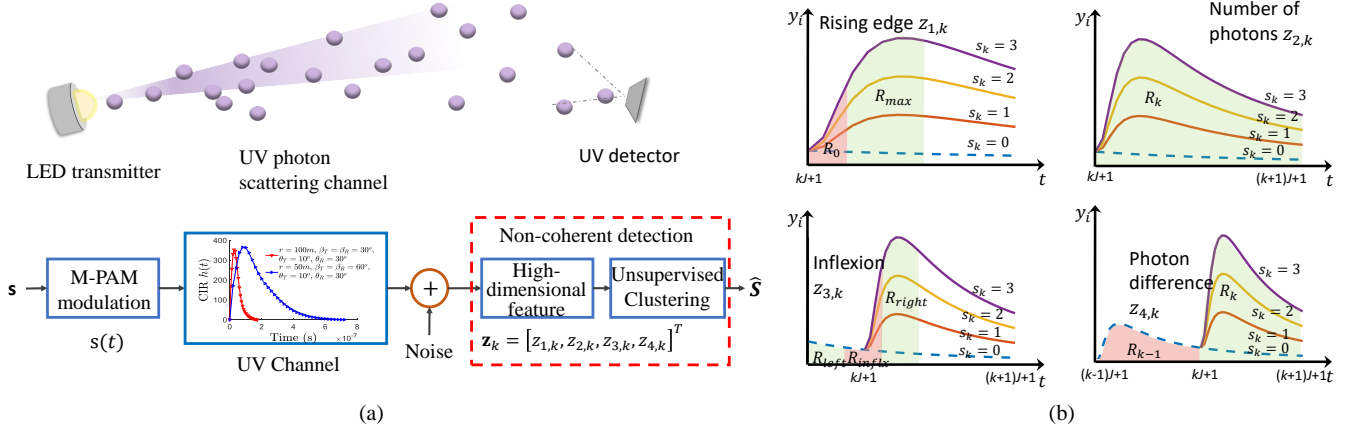


Fig. 1. Schematic flow. a) illustrates the UVC system and the non-coherent detection scheme. b) shows the four UV sub-features: rising-edge, number of photons, inflexion, and photon difference, with respect to $M = 4$ -PAM modulation.

Here, $D = 4$ of our previously designed UV sub-features are used [23]:

$$z_{1,k} \triangleq \frac{1}{|\mathcal{R}_{\max}|} \sum_{i \in \mathcal{R}_{\max}} y_i - \frac{1}{|\mathcal{R}_0|} \sum_{i \in \mathcal{R}_0} y_i, \quad (4a)$$

$$z_{2,k} \triangleq \frac{1}{|\mathcal{R}_k|} \sum_{i \in \mathcal{R}_k} y_i, \quad (4b)$$

$$z_{3,k} \triangleq -\frac{1}{|\mathcal{R}_{\text{inflex}}|} \sum_{i \in \mathcal{R}_{\text{inflex}}} y_i + \frac{1}{2} \left(\frac{\sum_{i \in \mathcal{R}_{\text{left}}} y_i}{|\mathcal{R}_{\text{left}}|} + \frac{\sum_{i \in \mathcal{R}_{\text{right}}} y_i}{|\mathcal{R}_{\text{right}}|} \right), \quad (4c)$$

$$z_{4,k} \triangleq \frac{1}{|\mathcal{R}_k|} \sum_{i \in \mathcal{R}_k} y_i - \frac{1}{|\mathcal{R}_{k-1}|} \sum_{i \in \mathcal{R}_{k-1}} y_i, \quad (4d)$$

In Eq. (4a), the sub-feature $z_{1,k}$ is referred to the rising-edge of k th symbol-interval, whose value is ISI-insensitive but only depends on the different PAM input symbols s_k . $\mathcal{R}_{\max} \triangleq (k-1)J + \{i_{\max} - \lfloor J/4 \rfloor, \dots, i_{\max} + \lfloor J/4 \rfloor\}$ and $\mathcal{R}_0 \triangleq (k-1)J + \{1, \dots, \lfloor J/4 \rfloor\}$ are set to determine the related index areas for rising-edge computation. i_{\max} is the index corresponding to the maximum value of discrete CIR $[h_1, \dots, h_{+\infty}]$. We approximate i_{\max} using the index of the maximum value of the non-zero symbols related received signals in training data. Here, i_{\max} does not need to be very accurate, since \mathcal{R}_{\max} is defined to include the adjacent area of i_{\max} for rising edge computation. In Eq. (4b), $z_{2,k}$ is referred to as the number of received photons within k th symbol-interval, where $\mathcal{R}_k \triangleq \{(k-1)J + 1, \dots, kJ\}$. In Eq. (4c), $z_{3,k}$ accounts for the inflexion feature, whose value is also ISI-insensitive and increases with a larger symbol pulse s_k . Here, the inflexion feature is computed by the left and right neighbours' values subtracting the central area's values. We hereby define $\mathcal{R}_{\text{inflex}} \triangleq (k-1)J + \{-\lfloor J/4 \rfloor, \dots, \lfloor J/4 \rfloor\}$, $\mathcal{R}_{\text{left}} \triangleq (k-1)J + \{-\lfloor J/2 \rfloor, \dots, -\lfloor J/4 \rfloor - 1\}$, and $\mathcal{R}_{\text{right}} \triangleq (k-1)J + \{\lfloor J/4 \rfloor + 1, \dots, \lfloor J/2 \rfloor\}$. $z_{4,k}$ gives the received photon number difference between successive symbol intervals k and $k-1$.

From Eq. (4) and the corresponding sub-feature shapes in Fig. 1(b), each of the sub-features is able to transform the

received ISI contaminated signals y_i into a new detection-space that is insensitive to ISI. For instance, given a fixed ISI intensity and any of s_k , the expectations of $z_{k,1}$, $z_{k,2}$, $z_{k,3}$ and $z_{k,4}$ remain quasi-constant, as they reflect only the common geometric shapes of the UV signals (e.g., the rising edge and the inflexion). In this view, by stacking them into a HD signal feature, i.e., $\mathbf{z}_k = [z_{1,k}, \dots, z_{4,k}]^T$, we are able to counteract the ISI effect, and convert the sequential detection with ISI into an ISI-insensitive detection framework (see Fig. 3(b)). Also, differing from the previous 1D feature, i.e., $z_k = \sum_{d=1}^D z_{d,k}$ in [23], the HD feature \mathbf{z}_k can provide a HD decision surface and result in a lower SER for signal detection (we will show this in Section III. C and in Fig. 4).

With the help of the HD feature \mathbf{z}_k in Eqs. (3)-(4), we provide the likelihood PDF of \mathbf{z}_k conditioned on different M -PAM symbols $s_k = m \in \{0, 1, \dots, M-1\}$, i.e.,

$$p(\mathbf{z}_k | s_k = m) = \mathcal{N}(\mathbf{z}_k; \boldsymbol{\mu}_m, \boldsymbol{\Sigma}) \triangleq \frac{1}{\sqrt{(2\pi)^D \cdot \det(\boldsymbol{\Sigma})}} \exp \left(-0.5 (\mathbf{z}_k - \boldsymbol{\mu}_m)^T \boldsymbol{\Sigma}^{-1} (\mathbf{z}_k - \boldsymbol{\mu}_m) \right), \quad (5)$$

where $\boldsymbol{\mu}_m = [\mu_{1,m}, \dots, \mu_{D,m}]^T$ represents the expectation of $\mathbf{z}_k = [z_{1,k}, \dots, z_{D,k}]^T$ conditioned on $s_k = m$, $\boldsymbol{\Sigma}$ gives the covariance matrix (of size $D \times D$) among the total $D = 4$ features in Eq. (4), and $\det(\cdot)$ is the determinant operator of a matrix. As such, the signal detection process is converted to determining $\boldsymbol{\mu}_m$ and $\boldsymbol{\Sigma}$, and selecting $s_k \in \{0, \dots, M-1\}$ that corresponds to the maximal likelihood PDF $p(\mathbf{z}_k | s_k = m)$, which can be viewed as a clustering problem (see Fig. 3(b) for illustration).

B. Non-Coherent Signal Detection Design

After the derivation of the HD UV feature \mathbf{z}_k in Eqs. (4a-4d), and its probability distributions Eq. (5), we design the UV-feature constrained unsupervised detection method, aiming to determine the expectations $\boldsymbol{\mu}_m$ and the covariance matrix $\boldsymbol{\Sigma}$, via the unlabeled first I computed features, i.e., $\mathbf{z}_1, \dots, \mathbf{z}_I$.

1) *Initialization*: The initialization of $\boldsymbol{\mu}_m$ leverages the increasingly equal difference characteristics, i.e., $\boldsymbol{\mu}_{m-1} -$

$2\mu_m + \mu_{m+1} = \mathbf{0}$. This is because the increasingly equal difference among the M -PAM symbols, i.e., $\{0, 1, \dots, M-1\}$, remains after passing through the LTI signal model in Eq. (2), and the linear sub-feature constructions in Eq. (4). Here, we characterize this increasingly equal difference by the following equations:

$$[\mu_0, \dots, \mu_{M-1}] \cdot \Psi = \mathbf{0}, \quad \mu_m \prec \mu_{m+1} \quad (6)$$

$$\Psi \triangleq \begin{bmatrix} 1 & -2 & 1 & 0 & 0 & \dots & 0 \\ 0 & 1 & -2 & 1 & 0 & \dots & 0 \\ & & & \vdots & & & \\ 0 & 0 & \dots & 0 & 1 & -2 & 1 \end{bmatrix}^T. \quad (7)$$

where \prec is the elemental-wise less than operator, and matrix Ψ of size $M \times (M-2)$ to ensure the equal difference.

The initialization of μ_m , denoted as $\mu_m^{(0)} = [\mu_{1,m}^{(0)}, \dots, \mu_{D,m}^{(0)}]^T$ is to implement Eqs. (6)-(7) via the first I (unlabelled) features, i.e.,

$$z_{d,k_1} < \dots < z_{d,k_I}, \text{ with } \{k_1, \dots, k_I\} = \{1, \dots, I\} \quad (8a)$$

$$\mathcal{I}_{d,m} = \{k_{(m-1)I/M+1}, \dots, k_{mI/M}\}, \quad (8b)$$

$$c_{d,m} = \frac{1}{|\mathcal{I}_{d,m}|} \sum_{k \in \mathcal{I}_{d,m}} z_{d,k}, \quad \mathbf{c}_m = [c_{1,m}, \dots, c_{D,m}]^T. \quad (8c)$$

$$[\mu_0^{(0)}, \dots, \mu_{M-1}^{(0)}] = [\mathbf{c}_0, \dots, \mathbf{c}_{M-1}] ([\varphi_1, \varphi_2]^\dagger)^T [\varphi_1, \varphi_2]^T. \quad (8d)$$

Here, Eq. (8a) is to re-order the first I sub-features $z_{d,1}, \dots, z_{d,I}$ into an ascending order. Eqs. (8b)-(8c) are to assign M sets (clusters) given the ascending order of z_{d,k_i} , and compute each cluster's centre (mean). Eq. (8d) is to ensure the increasingly equal difference of μ_0, \dots, μ_{M-1} , or saying to ensure $[\mu_0^{(0)}, \dots, \mu_{M-1}^{(0)}]^T$ in the null-space of Ψ according to Eq. (6). We do so by firstly computing the null-space of Ψ^T (of size $(M-2) \times M$), i.e., its two eigenvectors φ_1 and φ_2 corresponding to 0 eigenvalue. Then, we use the null-space basis to approximate the centre of each set by the least square error (LSE), and assign the approximation as the initialization. As such, the initial $[\mu_0^{(0)}, \dots, \mu_{M-1}^{(0)}]$ can be computed as Eq. (8d) following the increasingly equal difference and also located around the centres of the feature set.

2) *Constrained Learning*: After the initialization of μ_m , we adopt the Gaussian mixture model (GMM) clustering framework to identify the expectation μ_m and the covariance Σ of the UV feature $\mathbf{z}_k | (s_k = m)$ in Eq. (5). In essence, GMM clustering is to maximize the the log-likelihood, i.e.,

$$\max_{\mu_{0:M-1}, \Sigma} \mathcal{L}(\mathbf{z}_{1:I} | \mu_{0:M-1}, \Sigma), \quad (9)$$

where $\mathbf{z}_{1:I} \triangleq [\mathbf{z}_1, \dots, \mathbf{z}_I]$, $\mu_{0:M-1} \triangleq [\mu_0, \dots, \mu_{M-1}]$. For this work, $\mathcal{L}(\mathbf{z}_{1:I} | \mu_{0:M-1}, \Sigma)$ is computed as:

$$\mathcal{L}(\mathbf{z}_{1:I} | \mu_{0:M-1}, \Sigma) = \sum_{k=1}^I \log \sum_{m=0}^{M-1} \mathcal{N}(\mathbf{z}_k | \mu_m, \Sigma) \\ = \sum_{k=1}^I \log \sum_{m=0}^{M-1} w_{k,m} \frac{\mathcal{N}(\mathbf{z}_k | \mu_m, \Sigma)}{w_{k,m}} \quad (10a)$$

$$\geq \sum_{k=1}^I \sum_{m=0}^{M-1} w_{k,m} \log \frac{\mathcal{N}(\mathbf{z}_k | \mu_m, \Sigma)}{w_{k,m}} \quad (10b)$$

$$= \sum_{k=1}^I \sum_{m=0}^{M-1} w_{m,k} \left(-\log(w_{m,k}) - \frac{1}{2} \log(\Sigma) \right) \\ - \sum_{k=1}^I \sum_{m=0}^{M-1} w_{m,k} \left(\frac{1}{2} (\mathbf{z}_k - \mu_m)^T \Sigma^{-1} (\mathbf{z}_k - \mu_m) \right). \quad (10c)$$

In Eq. (10), $w_{m,k}$ is referred to as a hidden variable. Eq. (10b) is due to the Jensen inequality and concavity of logarithms, where equality holds if $\mathcal{N}(\mathbf{z}_k | \mu_m, \Sigma)/w_{k,m}$ is constant, i.e., $w_{m,k} = \mathcal{N}(\mathbf{z}_k | \mu_m, \Sigma) / \sum_{m=0}^{M-1} \mathcal{N}(\mathbf{z}_k | \mu_m, \Sigma)$. Then, the maximization problem in Eqs. (9)-(10) can be pursued via the expectation maximization (EM) algorithm, i.e., [29], [30]

$$w_{m,k}^{(j)} = \frac{\mathcal{N}(\mathbf{z}_k | \mu_m^{(j)}, \Sigma^{(j)})}{\sum_{m=0}^{M-1} \mathcal{N}(\mathbf{z}_k | \mu_m^{(j)}, \Sigma^{(j)})}, \quad (11a)$$

$$\mu_m^{(j+1)} = \frac{\sum_{k=1}^I w_{m,k}^{(j)} \cdot \mathbf{z}_k}{\sum_{k=1}^I w_{m,k}^{(j)}}, \quad (11b)$$

$$\Sigma^{(j+1)} = \frac{\sum_{m=0}^{M-1} \sum_{k=1}^I w_{m,k}^{(j)} (\mathbf{z}_k - \mu_m^{(j+1)})^T \cdot (\mathbf{z}_k - \mu_m^{(j+1)})}{\sum_{m=0}^{M-1} \sum_{k=1}^I w_{m,k}^{(j)}}. \quad (11c)$$

where j is the iteration step. Eq. (11a) refers to the E-step, which rises the previous j th iteration maximized lower-bound to the original log-likelihood, by equalizing the Jensen Inequality. Eqs. (11b)-(11c) are to maximize the lower-bound in Eq. (10c) given the fixed hidden variable $w_{k,m}^{(j)}$. As such, an optimal (local or global) solution of μ_m and Σ can be obtained by iteration using Eqs. (11a)-(11c).

However, it is noteworthy that directly using Eq. (11) may fall into a local optimal solution, due to the likelihood approximation by Jensen's inequality and the following successive optimization steps [29], [30]. We illustrate this in Fig. 2.

To avoid such local optimal solutions, we propose to exploit the properties of the extracted UV features, and convert Eq. (11b) into a convex problem. We do so, by re-writing the objective function corresponding to μ_m (the second term in Eq. (10c)), and then adding convex constraints in accordance with the characteristics of the UV features. The second term in Eq. (10c) can be re-written as:

$$- \sum_{k=1}^I \sum_{m=0}^{M-1} w_{m,k} \left(\frac{1}{2} (\mathbf{z}_k - \mu_m)^T \Sigma^{-1} (\mathbf{z}_k - \mu_m) \right) \\ = - \sum_{k=1}^I \text{tr} \left(\mathbf{W}_k (\mathbf{Z}_k - \mathbf{U})^T \Sigma^{-1} (\mathbf{Z}_k - \mathbf{U}) \right), \quad (12)$$

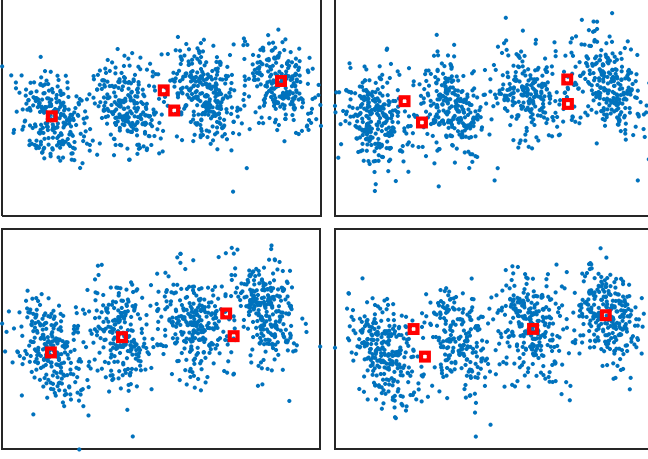


Fig. 2. Illustration of clustering errors using classic GMM in Eq. (11): four cases of GMM trapped in local optimal solutions.

Algorithm 1 Non-Coherent Signal Detection Algorithm

Input: Received UV signals y_1, \dots, y_{KN} , modulation type M -PAM, and number of features I for unsupervised training.

- 1: $\forall k \in \{1, \dots, K\}$, compute HD UV feature \mathbf{z}_k via Eqs. (3)-(4).
- 2: Initialize $\mu_m^{(0)}$ via Eq. (8).
- 3: Assign $j = 0$ and $\Delta^{(j)} = \|\mu_1^{(j)}, \dots, \mu_{M-1}^{(j)}\|_{\text{fro}}$.
- 4: **while** $\Delta^{(j)} > \epsilon$ **do**
- 5: Compute $w_{m,k}^{(j)}$ via Eq. (11a).
- 6: Assign $j = j + 1$.
- 7: Update μ_m by solving convex problem in Eq. (13).
- 8: Update $\Sigma^{(j)}$ via Eq. (11c).
- 9: $\Delta^{(j)} = \|\mu_1^{(j)}, \dots, \mu_{M-1}^{(j)} - [\mu_1^{(j-1)}, \dots, \mu_{M-1}^{(j-1)}]\|_{\text{fro}}$
- 10: **end while**
- 11: Assign $\mu_m = \mu_m^{(j)}$, and $\Sigma = \Sigma^{(j)}$.
- 12: **for** $k \in \{1, \dots, K\}$ **do**
- 13: Determine the M -PAM symbol \hat{s}_k via Eq. (14).
- 14: **end for**

Output: Return the detected symbol $\hat{s}_1, \dots, \hat{s}_K$.

where $\mathbf{W}_k \triangleq \text{diag}([w_{0,k}, \dots, w_{M-1,k}]^T)$ is the diagonal matrix from vector $[w_{0,k}, \dots, w_{M-1,k}]^T$, $\mathbf{Z}_k \triangleq [\mathbf{z}_k, \dots, \mathbf{z}_k]$ reproduces M times the vector \mathbf{z}_k , $\mathbf{U} \triangleq [\mu_0, \dots, \mu_{M-1}]$, and $\text{tr}(\cdot)$ gives the trace operator of a matrix. Then, the maximization problem over $\mu_{0:M-1}$ in Eq. (11b) can be converted to the following convex problem with UV signal related constraints:

$$\min_{\mathbf{U}} \sum_{k=1}^I \text{tr}(\mathbf{W}_k (\mathbf{Z}_k - \mathbf{U})^T \Sigma^{-1} (\mathbf{Z}_k - \mathbf{U})) \quad (13a)$$

$$\text{s.t. } \|\mathbf{U}\Psi\|_F^2 < \gamma, \quad (13b)$$

$$\mathbf{c}_d^T \mathbf{U} \mathbf{b} = \mu_{d,M-1} - \mu_{d,0} > 0, \quad \forall d \in \{1, \dots, D\}, \quad (13c)$$

$$\mathbf{c}_1^T \mathbf{U} \mathbf{b} = \mu_{1,M-1} - \mu_{1,0} < \max_{1 \leq k, k' \leq I} \{z_{1,k} - z_{1,k'}\}, \quad (13d)$$

$$\mathbf{c}_1^T \mathbf{U} \mathbf{b} = \mu_{1,M-1} - \mu_{1,0} > 0.5 \left(\mu_{1,M-1}^{(0)} - \mu_{1,0}^{(0)} \right) \quad (13e)$$

Eq. (13a) is the objective function. Eq. (13b) is to ensure the equal difference expressed in Eq. (6), by making the squared

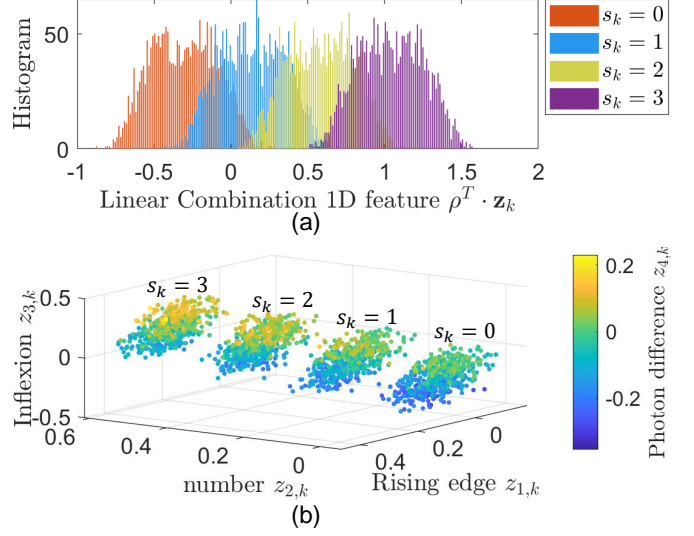


Fig. 3. Illustration of non-coherent schemes that transform the ISI caused sequential detection space into an ISI-released multi-hypothesis detection framework. Under the same received UV signals, (a) shows the poor detection accuracy from 1D non-coherent schemes, (b) gives the higher detection accuracy of the proposed HD non-coherent scheme (as proved by Section III. C).

Frobenius norm of $\mathbf{U}\Psi$, i.e., $\|\mathbf{U}\Psi\|_F^2$, less than some small γ . Eqs. (13c)-(13e) are to confine the differences between the expectations (clustering centres), where Eq. (13c) is to assign μ_{M-1} and μ_0 corresponding to the largest and smallest symbols, respectively. Eqs. (13d)-(13e) are to confine the difference of the expectation of the rising-edge with respect to the largest and the smallest symbols.

After the derivation of μ_m and Σ , the signal detection process can be pursued by computing and comparing the logarithm-form of the conditioned likelihood PDF, i.e.,

$$\hat{s}_k = \underset{m \in \{0, \dots, M-1\}}{\text{argmax}} -(\mathbf{z}_k - \mu_m)^T \Sigma^{-1} (\mathbf{z}_k - \mu_m). \quad (14)$$

3) Overall Non-Coherent Detection Algorithm: After the elaboration of the HD non-coherent detection scheme designed, we provide a algorithm flow in Algo. 1. The inputs are the received UV signals, the modulation type M , and the number of features I for unsupervised learning. Step 1 is to compute the HD feature \mathbf{z}_k from the received signals for each symbol. Steps 2-11 are to learn the expectations μ_m and the covariance matrix Σ for the conditioned likelihood PDF of \mathbf{z}_k . Steps 12-14 are to pursue the signal detection for an M -PAM symbol. Here, we assign $\epsilon = 10^{-3}$ as the terminal condition. Below this ϵ , the clustering points and the co-variance matrix will not change drastically, and these changes will not have a significant influence on the further clustering (detection) results.

4) Convergence Analysis: We then analyze the convergence of the proposed scheme in Algo. 1. We prove this by showing that the objective log-likelihood function in Eq. (10) is non-decreasing from iteration j to iteration $j+1$, i.e., $\mathcal{L}(\mathbf{z}_{1:I} | \mu_{0:M-1}^{(j)}, \Sigma^{(j)}) \leq \mathcal{L}(\mathbf{z}_{1:I} | \mu_{0:M-1}^{(j+1)}, \Sigma^{(j+1)})$. This can

be illustrated by following relationships:

$$\begin{aligned} \mathcal{L}(\mathbf{z}_{1:I}|\boldsymbol{\mu}_{0:M-1}^{(j)}, \boldsymbol{\Sigma}^{(j)}) &= \sum_{k=1}^I \log \sum_{m=0}^{M-1} \mathcal{N}(\mathbf{z}_k|\boldsymbol{\mu}_m^{(j)}, \boldsymbol{\Sigma}^{(j)}) \\ &= \sum_{k=1}^I \log \sum_{m=0}^{M-1} w_{k,m}^{(j)} \frac{\mathcal{N}(\mathbf{z}_k|\boldsymbol{\mu}_m^{(j)}, \boldsymbol{\Sigma}^{(j)})}{w_{k,m}^{(j)}} \end{aligned} \quad (15a)$$

$$= \sum_{k=1}^I \sum_{m=0}^{M-1} w_{k,m}^{(j)} \log \frac{\mathcal{N}(\mathbf{z}_k|\boldsymbol{\mu}_m^{(j)}, \boldsymbol{\Sigma}^{(j)})}{w_{k,m}^{(j)}} \quad (15b)$$

$$\begin{aligned} &= \sum_{k=1}^I \sum_{m=0}^{M-1} w_{m,k}^{(j)} \left(-\log(w_{m,k}^{(j)}) - \frac{1}{2} \log(\boldsymbol{\Sigma}^{(j)}) \right) \\ &\quad - \sum_{k=1}^I \sum_{m=0}^{M-1} w_{m,k}^{(j)} \left(\frac{1}{2} (\mathbf{z}_k - \boldsymbol{\mu}_m^{(j)})^T (\boldsymbol{\Sigma}^{(j)})^{-1} (\mathbf{z}_k - \boldsymbol{\mu}_m^{(j)}) \right) \end{aligned} \quad (15c)$$

$$\begin{aligned} &\leq \sum_{k=1}^I \sum_{m=0}^{M-1} w_{m,k}^{(j)} \left(-\log(w_{m,k}^{(j)}) - \frac{1}{2} \log(\boldsymbol{\Sigma}^{(j)}) \right) \\ &\quad - \sum_{k=1}^I \sum_{m=0}^{M-1} w_{m,k}^{(j)} \left(\frac{1}{2} (\mathbf{z}_k - \boldsymbol{\mu}_m^{(j+1)})^T (\boldsymbol{\Sigma}^{(j)})^{-1} (\mathbf{z}_k - \boldsymbol{\mu}_m^{(j+1)}) \right) \end{aligned} \quad (15d)$$

$$\begin{aligned} &\leq \sum_{k=1}^I \sum_{m=0}^{M-1} w_{m,k}^{(j)} \left(-\log(w_{m,k}^{(j)}) - \frac{1}{2} \log(\boldsymbol{\Sigma}^{(j+1)}) \right) \\ &\quad - \sum_{k=1}^I \sum_{m=0}^{M-1} w_{m,k}^{(j)} \left(\frac{1}{2} (\mathbf{z}_k - \boldsymbol{\mu}_m^{(j+1)})^T (\boldsymbol{\Sigma}^{(j+1)})^{-1} (\mathbf{z}_k - \boldsymbol{\mu}_m^{(j+1)}) \right) \end{aligned} \quad (15e)$$

$$= \sum_{k=1}^I \sum_{m=0}^{M-1} w_{k,m}^{(j)} \log \frac{\mathcal{N}(\mathbf{z}_k|\boldsymbol{\mu}_m^{(j+1)}, \boldsymbol{\Sigma}^{(j+1)})}{w_{k,m}^{(j)}} \quad (15f)$$

$$\leq \sum_{k=1}^I \log \sum_{m=0}^{M-1} w_{k,m}^{(j)} \frac{\mathcal{N}(\mathbf{z}_k|\boldsymbol{\mu}_m^{(j+1)}, \boldsymbol{\Sigma}^{(j+1)})}{w_{k,m}^{(j)}} \quad (15g)$$

$$= \sum_{k=1}^I \log \sum_{m=0}^{M-1} \mathcal{N}(\mathbf{z}_k|\boldsymbol{\mu}_m^{(j+1)}, \boldsymbol{\Sigma}^{(j+1)}) = \mathcal{L}(\mathbf{z}_{1:I}|\boldsymbol{\mu}_{0:M-1}^{(j+1)}, \boldsymbol{\Sigma}^{(j+1)}) \quad (15h)$$

Eq. (15a) describes the computation of the log-likelihood objective function. Eq. (15b) holds for the equality condition in Jensen's inequality, i.e., $w_{k,m}^{(j)} = \mathcal{N}(\mathbf{z}_k; \boldsymbol{\mu}_m^{(j)}, \boldsymbol{\Sigma}^{(j)}) / \sum_{m=0}^{M-1} \mathcal{N}(\mathbf{z}_k; \boldsymbol{\mu}_m^{(j)}, \boldsymbol{\Sigma}^{(j)})$ (corresponding to step 5 in Algo. 1). Eq. (15c) is the expansion of Eq. (15b). Eq. (15d) holds since $\boldsymbol{\mu}_{0:M-1}^{(j+1)}$ is the optimal solution of the proposed convex problem, which maximizes Eq. (15c) given fixed $w_{k,m}^{(j)}$ and $\boldsymbol{\Sigma}^{(j)}$ (corresponding to step 7 in Algo. 1). Eq. (15e) holds since $\boldsymbol{\Sigma}^{(j+1)}$ is the optimal solution that maximizes Eq. (15d), given fixed $w_{k,m}^{(j)}$ and $\boldsymbol{\mu}_{0:M-1}^{(j+1)}$ (corresponding to step 8 in Algo. 1). Eq. (15f) is the direct computation from Eq. (15e). Eq. (15g) arises from Jensen's inequality, which then gives Eq. (15h). Meanwhile, it is noted that there always exists a maximum of the log-likelihood in the GMM clustering. As a consequence, combined with Eqs. (15a)-(15h), the convergence of the proposed non-coherent detection algorithm can be proved.

C. Theoretical Symbol Error Rate Analysis

After the unsupervised learning of the likelihood PDFs (i.e., with learned $\boldsymbol{\mu}_m$ and $\boldsymbol{\Sigma}$), we provide the theoretical SER of our proposed HD feature based non-coherent detection, and compare it with our previously proposed one-dimensional feature based non-coherent scheme in [23].

Similar to the binary case (e.g., OOK), the theoretical SER for the M -PAM symbol is expressed by the summation of the detection error probability for each symbol, i.e., $p(\hat{s}_k \neq m | s_k = m)$, which then can be expressed given the Gaussian type likelihood PDF in Eq. (3). As such, we provide the theoretical SER as follows:

$$\begin{aligned} SER(\mathbf{z}_k) &= \sum_{m=0}^{M-1} p(\hat{s}_k \neq m | s_k = m) \cdot Pr(s_k = m) \\ &= \frac{1}{M} \sum_{m=1}^{M-1} \Phi \left(-0.5 \sqrt{(\boldsymbol{\mu}_m - \boldsymbol{\mu}_{m-1})^T \boldsymbol{\Sigma}^{-1} (\boldsymbol{\mu}_m - \boldsymbol{\mu}_{m-1})} \right) \end{aligned} \quad (16)$$

where $\Phi(x) = \int_{-\infty}^x 1/\sqrt{(2\pi)} \exp(-u^2/2) du$ is the cumulative probability function (CDF) of the Normal distribution $\mathcal{N}(0, 1)$.

Then, we will prove that the proposed HD non-coherent detection can provide a lower SER as opposed to the 1D non-coherent scheme, i.e.,

$$SER(\mathbf{z}_k) < SER(\boldsymbol{\rho}^T \cdot \mathbf{z}_k), \quad (17)$$

where the latter is the SER of the 1D non-coherent scheme with $\boldsymbol{\rho} = [\rho_1, \dots, \rho_D]^T$ the optimal weights [23]. By taking Eq. (16) into Eq. (17) and using the monotonically increasing property of $\Phi(x)$, we prove a more strict inequality as follows:

$$\mathbf{x}^T \cdot \left(\boldsymbol{\Sigma}^{-1} - \boldsymbol{\rho} (\boldsymbol{\rho}^T \boldsymbol{\Sigma} \boldsymbol{\rho})^{-1} \boldsymbol{\rho}^T \right) \cdot \mathbf{x} \geq 0, \quad (18)$$

where $\mathbf{x} = \boldsymbol{\mu}_m - \boldsymbol{\mu}_{m-1}$, $\forall m \in \{0, \dots, M-1\}$. Given the symmetric positive definite property of the covariance matrix $\boldsymbol{\Sigma}$, we have the eigenvalue decomposition as $\boldsymbol{\Sigma} = \mathbf{Q} \cdot \text{diag}([\lambda_1, \dots, \lambda_D]^T) \cdot \mathbf{Q}^T$. Then, by assigning $\mathbf{v} = [v_1, \dots, v_D]^T = \mathbf{Q}^T \boldsymbol{\rho}$ and $\mathbf{y} = [y_1, \dots, y_D]^T = \mathbf{Q}^T \mathbf{x}$, we re-write the left-hand side of Eq. (18), and prove it no less than 0, i.e.,

$$\begin{aligned} &\mathbf{y}^T \cdot \left(\text{diag} \left(\left[\frac{1}{\lambda_1}, \dots, \frac{1}{\lambda_D} \right]^T \right) - \frac{\mathbf{v} \mathbf{v}^T}{\sum_{d \in \mathcal{D}} \lambda_d \cdot v_d^2} \right) \cdot \mathbf{y} \\ &= \sum_{d \in \mathcal{D}} \sum_{d' \in \mathcal{D} \setminus \{d\}} \lambda_{d'} v_{d'}^2 \cdot \frac{y_d^2}{\lambda_d} - 2 \sum_{d, d' \in \mathcal{D}, d \neq d'} v_d v_{d'} y_d y_{d'} \\ &= \sum_{d, d' \in \mathcal{D}, d \neq d'} \left(\frac{\lambda_{d'} v_{d'}}{\lambda_d} y_d - \frac{\lambda_d v_d}{\lambda_{d'}} y_{d'} \right)^2 \geq 0. \end{aligned} \quad (19)$$

As such, we have proved theoretically that our proposed HD feature based non-coherent detection scheme has a lower SER than the 1D non-coherent scheme. We will further demonstrate this in Fig. 3, and via Section IV below.

IV. NUMERICAL SIMULATIONS

In this section, we evaluate the performance of our proposed HD non-coherent detection scheme. We measure the detection

accuracy via the BER. The computational complexity is represented by the number of multiplication operations required.

For the UV channel modelling, we adopt the Monte-Carlo techniques proposed by [10], [11], to obtain the discrete CIR coefficients in Eq. (2). The relevant channel parameters are configured as follows, which are typical and consistent with the studies in [21], [23]. The number of emitted photons for a single symbol-unit (i.e., $s_k = 1$) is $N_T = 10^{10}$, over a transmission distance between Tx and Rx of $r = 500\text{m}$. We set Tx's beam divergence and apex angle to be $\theta_T = \pi/12$ and $\beta_T = \pi/4$, and Rx's half-field of view and apex angle to be $\theta_R = \pi/12$ and $\beta_R = \pi/4$. The atmospheric coefficients are $\kappa_a = \kappa_s = 5 \times 10^{-4}\text{m}^{-1}$. For simulating different ISI intensities, we set the range of the symbol interval as $T_b \in [10^6, 5 \times 10^6\text{bit/s}]$ (with units of μs). The SNR is assigned to range from 5dB to 25dB to illustrate the BER versus different levels of ambient noise.

For comparison, we select the 1D non-coherent scheme [23], the minimum mean square error (MMSE) based linear equalizer as a benchmark, and the state-of-the-art coherent MLSD using least square (LS) channel estimator and Viterbi detection algorithm [19]. We aim to demonstrate our BER proximity to that of MLSD, but at a lower computational complexity given the exploitation of the HD ISI-intensive features. For fairness, the number of samples during one symbol interval T_b is assigned as $J = 10$ for all three schemes.

A. Communication Accuracy

We evaluate the detection accuracy of our proposed HD non-coherent detection scheme in Figs. 4-6. Fig. 4 provides the BER comparison of the four schemes versus different levels of SNR, under OOK modulation (given that the compared schemes in [19], [23] were designed only for OOK). It is observed from Fig. 4 that, the proposed HD non-coherent detection scheme outperforms the previous 1D non-coherent scheme (a gain of 5dB in SNR). This matches the theoretical error analysis in Section III. C. The theoretical BER of the proposed scheme is also provided, which gives a tight lower-bound of numerical simulations. A small gap can be found between the theoretical and the simulated curves, especially in the low SNR region. This is because the training errors in our designed clustering method become worse as the SNR decreases. Then, it is seen from Fig. 4 that the BER of our proposed HD non-coherent scheme is lower than that of the MMSE equalizer benchmark, and is close to the state-of-the-art MLSD. For example, a 1dB gap can be achieved when the BER reaches the 7% overhead hard-decision forward error correction (FEC) limit (i.e., $\text{BER} = 4.5 \times 10^{-3}$) [31], which suggests a comparable error-free communication performance with MLSD method when adopting an appropriate FEC code. This is attributed to the exploration of the ISI-insensitive UV features (e.g., rising edge, inflexion), which are able to inherently counteract the ISI effect, and are thereby offer a remarkable detection performance.

Fig. 5 illustrates the BER comparisons versus the different intensities of the ISI effect. Here, we use a range of symbol rates (i.e., $R_s \in [10^6, 1.5 \times 10^7]$ bit/s) to reflect the different

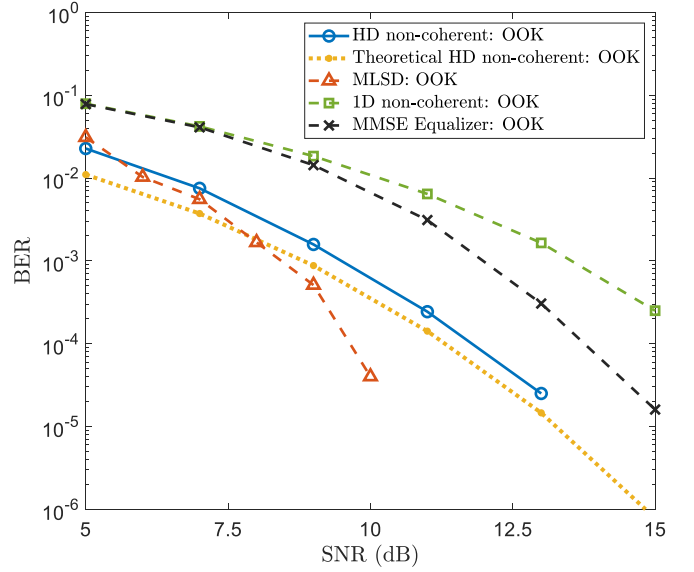


Fig. 4. BER comparison versus SNR under OOK modulation. Our proposed HD non-coherent detection outperforms the MMSE equalizer and the previous 1D non-coherent scheme, and approaches that of the MLSD method.

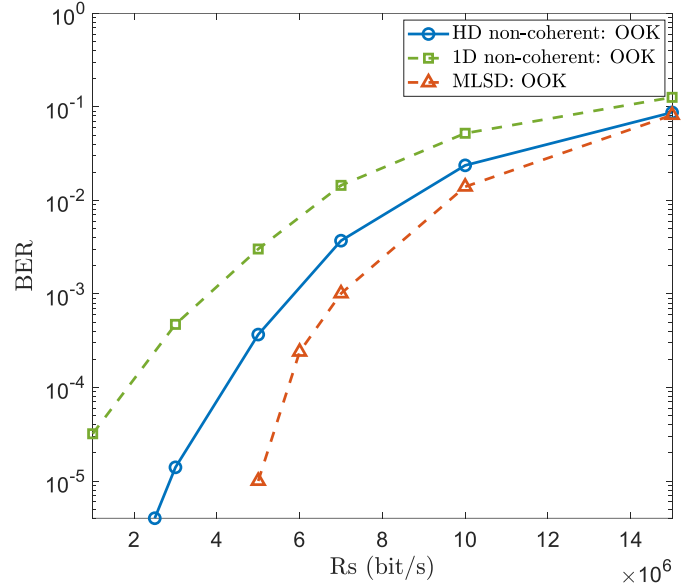


Fig. 5. BER comparison versus ISI (rendered by different symbol rates R_s), under OOK modulation. The result suggests the robustness of our proposed HD non-coherent detection scheme to different ISI intensities and approaches that of the MLSD method.

intensities of ISI, as a higher symbol rate will introduce a more severe ISI and will then negatively impact the performance of the communication system more significantly. We can observe from Fig. 5 that with the growth of the ISI intensities (i.e., the increase of symbol rate R_s), the BERs of all schemes become larger, showing that the ISI induced by the NLoS UV scattering effect causes deterioration in the communication performance. For comparison among these schemes, two similar results are obtained. Firstly, the HD non-coherent scheme outperforms the 1D non-coherent scheme, which matches the proof in Section III. C. Secondly, the proposed scheme can

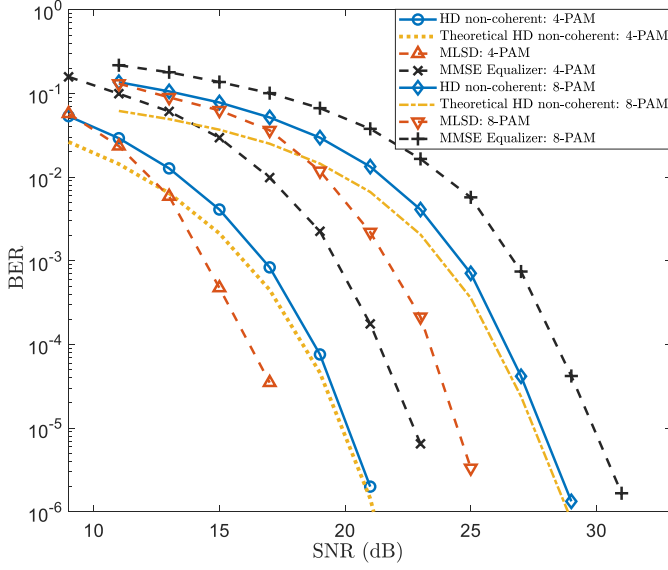


Fig. 6. BER versus SNR under $M = 4, 8$ -PAM symbol. Our proposed scheme shows comparable accuracy with the MLSD and MMSE equalizer, suggesting its suitability for multi-symbol UVC scenarios.

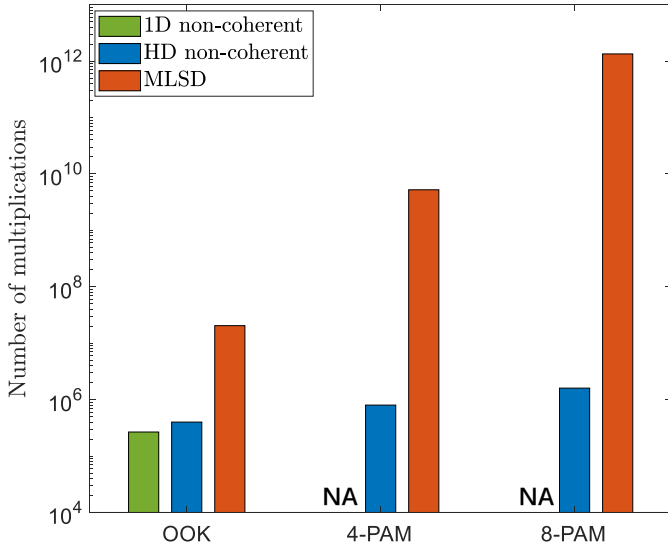


Fig. 7. Computational complexity comparison with the MLSD method, emphasizing the computational efficiency of our proposed HD non-coherent scheme.

approach the state-of-the-art MLSD method, given its ability to transform (approximate) the ISI caused sequential detection space into the ISI-released detection framework (see Fig. 3(b)).

Fig. 6 shows the performance of our proposed scheme for M -PAM modulation. Here, we only compare it with the MMSE equalizer and the MLSD requiring an M^L searching space, as the 1D non-coherent scheme in [23] cannot address the $M > 2$ -PAM situation. We can firstly see that, similar to the OOK case, the deduced theoretical BER serves as a very tight lower-bound. The gap between them is induced by training errors, which are worse in the low SNR region, but tolerable with high SNR. Then, it is observed that for the $M > 2$ symbol cases, our approach outperforms the benchmark provided by the MMSE equalizer, and shows a

comparable BER accuracy with the MLSD method. This, combined with the previous OOK simulation results, demonstrates both the reliability and the robustness of our proposed scheme, which is suitable for different signal modulation schemes in UVC systems combating ISI distortion.

B. Complexity Comparison

After the demonstration of the comparable communication accuracy with the state-of-the-art MLSD, we will show that our proposed HD non-coherent scheme demands a smaller amount of computational complexity. We measure the computational complexity via the number of multiplications. For our proposed HD non-coherent scheme, the number of multiplications in the detection process in Eq. (14) is $M \cdot (D^2 + D) \cdot N = O(MD^2N)$. The detection process for MLSD has an order of $O(LM^L N)$ multiplications (L is the length of ISI). For the previous 1D non-coherent scheme, only $M = 2$ -PAM (i.e., OOK) modulated signal can be detected and the number of multiplications has an order of $O(D^2N)$ [23]. To further compare the computational complexity in UV communications, Fig. 7 provides a comparison of the multiplication numbers for different schemes, under $D = 4$ sub-features, $N = 10^4$ transmitted symbols, and the length of ISI $L = 8$, for $M = 2, 4, 8$ -PAM. We can see that the proposed scheme has a very similar order of computational complexity to the previous 1D non-coherent scheme, but a significantly smaller order when compared to the MLSD. For OOK modulation, this gap is $2 \times (4^2 + 4) \times 10^4 = 4 \times 10^5 < 8 \times 2^8 \times 10^4 = 2 \times 10^7$, which, however, increases drastically for $M = 4, 8$ -PAM modulation (i.e., $4 \times (4^2 + 4) \times 10^4 = 8 \times 10^5 < 8 \times 4^8 \times 10^4 = 5.2 \times 10^9$, and $8 \times (4^2 + 4) \times 10^4 = 1.6 \times 10^6 < 8 \times 8^8 \times 10^4 = 1.3 \times 10^{12}$). As such, by combining the results from Figs. 4-7, we conclude that our proposed HD non-coherent scheme can provide a low-complexity based detection paradigm as well as comparable communication accuracy with the state-of-the-art coherent MLSD method.

V. CONCLUSION

For most optical wireless communications, signal detection with intensive ISI is extremely difficult. Current coherent schemes require high computational consumption, and non-coherent schemes cannot guarantee reliable detection accuracy. In this work, we have proposed a HD feature based non-coherent detection scheme, relying on the HD construction of four ISI-insensitive UV signals' sub-features, which has the following two merits. Firstly, it transforms the ISI caused sequential detection into the ISI-released multi-hypothesis detection framework, therefore avoiding high computational CIR estimation and sequential likelihood computations required by coherent schemes (a reduction of at least 2 orders of magnitude of complexity is achieved). Secondly, compared with previous 1D non-coherent schemes, the proposed HD feature based detection has been proved to provide a lower BER for signal detection, which is close to the detection accuracy of the state-of-the-art coherent MLSD ($< 1\text{dB}$ in SNR at the FEC limit $\text{BER} = 4.5 \times 10^{-3}$). These thereby demonstrate the promising pathway of the proposed non-coherent scheme towards a

low-computational but high-accuracy detection paradigm for optical wireless communications with intensive ISI.

REFERENCES

- [1] A. Vavoulas, H. G. Sandalidis, N. D. Chatzidiamantis, Z. Xu, and G. K. Karagiannidis, "A survey on ultraviolet C-Band (UV-C) communications," *IEEE Commun. Surveys Tut.*, vol. 21, no. 3, pp. 2111–2133, thirdquarter 2019.
- [2] R. J. Drost and B. M. Sadler, "Survey of ultraviolet non-line-of-sight communications," *Semicond. Sci. Tech.*, vol. 29, no. 8, p. 084006, Jun. 2014.
- [3] D. Kedar and S. Arnon, "Subsea ultraviolet solar-blind broadband free-space optics communication," *Opt. Eng.*, vol. 48, no. 4, p. 046001, Apr. 2009.
- [4] M. A. El-Shimy and S. Hranilovic, "Binary-input non-line-of-sight solar-blind UV channels: Modeling, capacity and coding," *J. Opt. Commun. Netw.*, vol. 4, no. 12, pp. 1008–1017, Dec. 2012.
- [5] Z. Xu and B. M. Sadler, "Ultraviolet communications: potential and state-of-the-art," *IEEE Commun. Mag.*, vol. 46, no. 5, pp. 67–73, May 2008.
- [6] G. A. Shaw, A. M. Siegel, and M. L. Nischan, "Demonstration system and applications for compact wireless ultraviolet communications," in *Sensors, and Command, Control, Communications, and Intelligence (C3I) Technologies for Homeland Defense and Law Enforcement II*, vol. 5071. International Society for Optics and Photonics, Sep. 2003, pp. 241–252.
- [7] K.-X. Sun, B. Allard, S. Buchman, S. Williams, and R. L. Byer, "LED deep UV source for charge management of gravitational reference sensors," *Classical Quant. Gravity*, vol. 23, no. 8, p. S141, Mar. 2006.
- [8] B. Albrecht, S. Kopta, O. John, M. Rütters, M. Kunzer, R. Driad, N. Marengo, K. Köhler, M. Walther, and O. Ambacher, "Improved AlGaIn pin photodetectors for monitoring of ultraviolet radiation," *IEEE J. Sel. Topics Quantum Electron.*, vol. 20, no. 6, pp. 166–172, May 2014.
- [9] H.-Y. Liu, W.-C. Hsu, B.-Y. Chou, and Y.-H. Wang, "Fabrication AlGaIn/GaN MIS UV photodetector by H₂O₂ oxidation," *IEEE Photon. Technol. Lett.*, vol. 27, no. 1, pp. 101–104, Oct. 2014.
- [10] H. Ding, G. Chen, A. K. Majumdar, B. M. Sadler, and Z. Xu, "Modeling of non-line-of-sight ultraviolet scattering channels for communication," *IEEE J. Sel. Area Commun.*, vol. 27, no. 9, pp. 1535–1544, Dec. 2009.
- [11] R. J. Drost, T. J. Moore, and B. M. Sadler, "UV communications channel modeling incorporating multiple scattering interactions," *J. Opt. Soc. Am. A.*, vol. 28, no. 4, pp. 686–695, Apr. 2011.
- [12] M. R. Luetgten, J. H. Shapiro, and D. M. Reilly, "Non-line-of-sight single-scatter propagation model," *J. Opt. Soc. Am. A.*, vol. 8, no. 12, pp. 1964–1972, Dec. 1991.
- [13] R. J. Drost, T. J. Moore, and B. M. Sadler, "Ultraviolet scattering propagation modeling: analysis of path loss versus range," *J. Opt. Soc. Am. A.*, vol. 30, no. 11, pp. 2259–2265, Nov. 2013.
- [14] M. A. Elshimy and S. Hranilovic, "Impact of finite receiver-aperture size in a non-line-of-sight single-scatter propagation model," *J. Opt. Soc. Am. A.*, vol. 28, no. 12, pp. 2568–2576, Dec. 2011.
- [15] S. Dimitrov, S. Sinanovic, and H. Haas, "Signal shaping and modulation for optical wireless communication," *Journal of Lightwave Technology*, vol. 30, no. 9, pp. 1319–1328, 2012.
- [16] W. Hu, M. Zhang, D. Han, Q. Chen, L. Ai, Q. Li, and Z. Ghassemlooy, "Research on channel-related polar code with an optimum code length for wireless ultraviolet communications," *Opt. Express*, vol. 25, no. 23, pp. 28 630–28 642, Nov. 2017.
- [17] X. Liang, M. Zhang, X. Li, L. Ai, and Z. Ghassemlooy, "Security performance of LDPC and polar codes in UV wireless communications," in *Proc. 1st West Asian Colloquium Opt. Wireless Commun., Isfahan, Iran*, Apr. 2018, pp. 1–6.
- [18] N. D. Chatzidiamantis, G. K. Karagiannidis, and M. Uysal, "Generalized maximum-likelihood sequence detection for photon-counting free space optical systems," *IEEE Trans. Commun.*, vol. 58, no. 12, pp. 3381–3385, Dec. 2010.
- [19] C. Gong and Z. Xu, "Channel estimation and signal detection for optical wireless scattering communication with inter-symbol interference," *IEEE Trans. Wireless Commun.*, vol. 14, no. 10, pp. 5326–5337, Oct. 2015.
- [20] Z. Wei, W. Hu, M. Zhang, D. Han, B. Li, and C. Zhao, "Viterbi estimation on the finite-state markov ultra-violet channels," in *Asia Communications and Photonics Conference (ACP)*, Nov. 2017, pp. 1–3.
- [21] Z. Wei, W. Hu, D. Han, M. Zhang, B. Li, and C. Zhao, "Simultaneous channel estimation and signal detection in wireless ultraviolet communications combating inter-symbol-interference," *Opt. Express*, vol. 26, no. 3, pp. 3260–3270, Feb. 2018.
- [22] D. Zou, C. Gong, and Z. Xu, "Signal detection under short-interval sampling of continuous waveforms for optical wireless scattering communication," *IEEE Trans. Wireless Commun.*, vol. 17, no. 5, pp. 3431–3443, May 2018.
- [23] W. Hu, Z. Wei, S. Popov, M. Leeson, M. Zhang, and T. Xu, "Non-Coherent Detection for Ultraviolet Communications with Inter-Symbol Interference," *Journal of Lightwave Technology*, vol. 38, no. 17, pp. 4699–4707, 2020.
- [24] Z. Wei, B. Li, W. Guo, W. Hu, and C. Zhao, "Sequential bayesian detection of spike activities from fluorescence observations," *IEEE Transactions on Molecular, Biological and Multi-Scale Communications*, vol. 5, no. 1, pp. 3–18, 2019.
- [25] X. Zhu and J. M. Kahn, "Free-space optical communication through atmospheric turbulence channels," *IEEE Trans. Commun.*, vol. 50, no. 8, pp. 1293–1300, Nov. 2002.
- [26] J. Li, J. Q. Liu, and D. P. Taylor, "Optical communication using subcarrier PSK intensity modulation through atmospheric turbulence channels," *IEEE Trans. Commun.*, vol. 55, no. 8, pp. 1598–1606, Aug. 2007.
- [27] M. L. B. Riediger, R. Schober, and L. Lampe, "Multiple-symbol detection for photon-counting MIMO free-space optical communications," *IEEE Trans. Wireless Commun.*, vol. 7, no. 12, pp. 5369–5379, Dec. 2008.
- [28] Z. Wei, W. Guo, B. Li, J. Charmet, and C. Zhao, "High-dimensional metric combining for non-coherent molecular signal detection," *IEEE Transactions on Communications*, vol. 68, no. 3, pp. 1479–1493, Mar. 2020.
- [29] G. Gan, C. Ma, and J. Wu, *Data clustering: theory, algorithms, and applications*. SIAM, 2020.
- [30] S. Borman, "The expectation maximization algorithm-a short tutorial," *Submitted for publication*, vol. 41, 2004.
- [31] F. Chang, K. Onohara, and T. Mizuochi, "Forward error correction for 100G transport networks," *IEEE Commun. Mag.*, vol. 48, no. 3, pp. S48–S55, Mar. 2010.